Biosensors and Bioelectronics 146 (2019) 111734

Contents lists available at ScienceDirect

Biosensors and Bioelectronics

journal homepage: http://www.elsevier.com/locate/bios

Synthesis of Zr-coordinated amide porphyrin-based two-dimensional covalent organic framework at liquid-liquid interface for electrochemical sensing of tetracycline

Xionghui Ma [a,*], Chaohai Pang [a], Shuhuai Li [a,**], Yuhao Xiong [b,***], Jianping Li [c], Jinhui Luo [a], Yan Yang [d]

[a] Hainan Provincial Key Laboratory of Quality and Safety for Tropical Fruits and Vegetables, Analysis and Test Center, Chinese Academy of Tropical Agricultural Sciences, Haikou, 571101, China
[b] College of Food and Bioengineering, Hezhou University, Hezhou, 542899, China
[c] Guangxi Key Laboratory of Electrochemical and Magnetochemical Function Materials, College of Chemistry and Bioengineering, Guilin University of Technology, Guilin, 541004, China
[d] Tropical Crops Genetic Resources Institute of Chinese Academy of Tropical Agricultural Sciences, Haikou, 571101, China

ARTICLE INFO

Keywords:
2D covalent organic framework
Electrocatalysis
Electrochemiluminescence
Liquid-liquid interface
Molecular imprinting
Zr

ABSTRACT

Highly-conductive two-dimensional covalent organic framework (COF) displays prominent applications in various fields of science and technology. This paper reports the design and liquid-liquid interface synthesis of a novel Zr-coordinated amide porphyrin-based 2D COF (Zr-amide-Por-based 2D COF). The COF adopts a graphene-like multilayer structure with the highest occupied molecular orbital (HOMO) and lowest unoccupied molecular orbital (LUMO) band gap of 1.6 eV. The ordered multilayer structure of the amide COF was confirmed through a series of characterization techniques, including scanning electron microscopy, high-resolution transmission electron microscopy, atomic force microscopy, Fourier-transform infrared spectroscopy, X-ray diffraction, and X-ray photoelectron spectroscopy. In particular, the inherent-ordered structure of Zr-amide-Por-based 2D COF with Zr as the catalytically active center confers several distinct advantages to the material, such as high conductivity and high electrocatalysis performance. A molecularly imprinted tetracycline electrochemiluminescence sensor was constructed based on the Zr-amide-Por-based 2D COF, and gate control effect was used as a signal-generation mechanism. Under optimal conditions, the sensor showed a good linear relationship with tetracycline in the concentration range of 5–60 pM, with a detection limit of 2.3 pM. Because the sensor is rapid, cost-efficient, highly sensitive, and specific, it can be considered as a viable platform for veterinary drug residue monitoring.

1. Introduction

Tetracycline (TC) is a broad-spectrum antibiotic for treatment against Gram-negative and Gram-positive bacterial infections in humans and animals and is used as an animal feed-additive owing to its low cost and high antibacterial activity (F. Li et al., 2019; Liu et al., 2018). However, the abuse of such antibacterial drugs in the animal industry has led to a series of problems. Antibiotic residues in food may adversely affect human health and cause bacterial resistance to TC in humans and animals. The maximum residue limits of TC in food recommended by the European Union in liver, kidney, egg, milk, and muscle tissue are 0.3, 0.6, 0.2, 0.1, and 0.1 mg/kg, respectively. Considering such low limits, the availability of sensitive and specific methods for detection of TC in foods is critical for its accurate analysis and to mitigate TC-resistance. Currently, the available analytical approaches for detection of TC include high-performance liquid chromatography (Cherkashina et al., 2018; Moudgil et al., 2019), liquid chromatography–mass spectrometry (Grande-Martínez et al., 2018; Guidi et al., 2018), capillary electrophoresis (Díaz-Quiroz et al., 2018; Moreno-González et al., 2018), and immunoassay (El Alami El Hassani et al., 2019; Sheng et al., 2018). While these analytical techniques have several merits, they typically require expensive and sophisticated equipment and involve long

* Corresponding author.
** Corresponding author.
*** Corresponding author.
E-mail addresses: maxionghui@foxmail.com (X. Ma), happylishuhuai@163.com (S. Li), xiongyuhao@yeah.net (Y. Xiong).

https://doi.org/10.1016/j.bios.2019.111734
Received 16 July 2019; Received in revised form 13 September 2019; Accepted 26 September 2019
Available online 29 September 2019

processing times; this highlights the need for the development of fast and simple TC detection methods with predictable applications. Electrochemical or optical sensors based on state-of-the-art nanomaterials, such as metal nanoparticles (Shahamirifard et al., 2018), metal-oxide nanomaterials (Shahamirifard and Ghaedi, 2019), carbon nanomaterials (Huang et al., 2016), polymer (Shumyantseva et al., 2016), and biomaterials (Zhang et al., 2018) have tremendously been employed as powerful analytical methods by captivating the benefit of easy-to-handle, cost-effective, highly sensitive and selective, rapid response, facile-to-fabricate and portable. Zhou et al., (2018) designed a dual-functional optical sensing of TC based on a highly stable luminescent Zr-based metal organic framework. In addition, electrochemical sensors based on molecular imprinting techniques or aptamers have gained increasing attention (Devkota et al., 2018). However, the sensitivity of these sensors must still be improved. Exploring a functionalized, high electron transfer efficiency electrode modification material is the key to improving the sensitivity of electrochemical sensors (Gao et al., 2016).

As a potential candidate, the covalent organic framework (COF) is a carbon-based nanoporous material with strong covalent bonds and has been widely used in the fields of energy storage (Yang et al., 2016), catalysis (Xiong et al., 2017, 2015), heavy-metal removal (Sun et al., 2017), and analytical chemistry (Zhang et al., 2018). Nevertheless, their poorly defined structures complicate characterization and hinder the further rational improvement of their characteristics. A conventional bulk COF as an electrode modification material is easy to fall off the electrode owing to its large particle size. Bulk COFs are very unfavorable for electron conduction due to a disorder structure, which seriously affects sensor performance. Additionally, the conventional hydrothermal synthesis of COF is time-consuming and involves preparation conditions, such as high temperatures and high pressures, which are not eco-friendly. While two-dimensional COF (2D COF) address these limitations by predictably and deliberately organizing redox-active groups into high-surface-area polymer networks with uniform micropores (Sahabudeen et al., 2016; Wang et al., 2019), their poor conductivity limits their electrochemical sensing application. Several strategies have thus been developed for improving the electrical conductivity of COF materials; these include the synthesis of 2D COF from the bottom-up self-assembly (Deblase et al., 2015), COF surface-coating conductive films (Mulzer et al., 2016), and unzipping (Ma et al., 2018). Despite their cumbersome and time-consuming synthesis challenges, 2D COFs hold significant promise in the development of fast, convenient, and highly conductive materials.

Interfacial reactions have emerged as desirable solutions for the preparation of 2D COF. The gas-liquid and liquid-liquid interfaces are the most common forms of interfacial polymerization. A variety of reactions, including Schiff-base condensation (Sahabudeen et al., 2016), Knoevenagel condensation (Wang et al., 2019), and Suzuki reaction (D. Zhou et al., 2018), have been applied in the interfacial synthesis of COF, and this continues to be a hot area of research with the use of several reactions for the construction of various kinds of functionalized 2D COF. The amide bond is a strong covalent bond and is widely used in the synthesis of conventional COF. However, the formation of a structurally ordered amide COF due to irreversible amide condensations remains a challenge when using amides in the preparation of COF (Khatioda et al., 2017; Liu et al., 2016). Stewart et al. (2017) reported on the synthesis of ordered amide COF with 2D and 3D covalent amide frameworks based on the diversification of amorphous polyamide network polymers under high-temperatures and -pressures. These reactions are expected to be useful for the preparation of ordered amide COF using liquid-liquid interfacial reactions. In this paper, we report on the successful synthesis of a novel Zr-coordinated amide porphyrin-based 2D COF (Zr-amide-Por-based 2D COF) by using a liquid-liquid interface assembly. The developed COF displayed unique and remarkable properties, such as strong catalytic effects and high electrical conductivity, which render it an ideal candidate for electrode modification. A simple and operationally convenient approach was undertaken for the development of an electrochemiluminescence (ECL) sensor, by employing a molecular imprinting technology (MIT) for fast and sensitive TC detection. As illustrated in Scheme 1a, the meso-tetra(4-carboxyphenyl)porphine (TcPP) was converted to its corresponding acid chloride, TcPP-chloride, which was then dissolved in dichloromethane to prepare an organic phase. An aqueous solution of *o*-phenylenediamine (*o*-PD) and $ZrCl_4$ was used as the aqueous phase. The organic phase was slowly added to the aqueous phase under a N_2 atmosphere to synthesize the Zr-amide-Por-based 2D COF through interfacial polymerization. As shown in Scheme 1b, the TC-molecularly imprinted electrochemiluminescence sensor (TC-MIECS) was prepared through electro-polymerization of *o*-PD as a functional monomer and TC as the molecular template on the surface of the COF-modified electrode. After removing the template molecule TC, imprinted cavities with specific recognition ability for tetracycline were obtained. During the determination process, the eluted sensor is placed in the sample solution for re-adsorption. Gate control with the luminol/hydrogen peroxide couple as the signal probe was employed as a signal-generation strategy (Li et al., 2015; Liu et al., 2017). As the TC concentration in the sample increases, the imprinted cavities are reoccupied, leading to an increase in the probe mass transfer resistance and resulting in a decrease in ECL intensity. The sensor's response signal was found to be inversely related to the TC concentration in the sample. Compared to conventional electrochemical sensors based on carbon-based porous materials, this work demonstrates several prominent advantages. 1) For the first time, amide 2D COFs were prepared through interfacial polymerization. Unlike conventional hydrothermal or sealing methods, interfacial polymerization is characterized by its facile operation and environmental friendliness. A 2D layered structure was obtained through a two-phase interface. The ultra-thin layered structure gives the material a strong adhesion, making it difficult to fall off from the electrode surface. 2) The highly ordered porous structure and the presence of metal active sites resulted in excellent electrical conductivity and electrocatalytic activity of the prepared 2D COF, resulting in an increase in the sensitivity of the constructed sensor. 3) Molecular imprinting techniques are used in 2D COFs-based ECL sensors. An identifiable selectivity increase was found for TC detection in a milk sample. Considering the many beneficial characteristics, the prepared COF is expected to be an ideal electrode surface modification material, with broad applicability in electrochemical sensing and electrocatalysis.

2. Materials and methods

2.1. Instrumentation and reagents

Electroanalytical measurements, such as cyclic voltammetry (CV) and electrochemical impedance spectroscopy (EIS), were performed on a CHI600E workstation (Shanghai Chenhua Instrument Co., Ltd., China) using a standard three-electrode system comprising an Ag/AgCl/Saturated KCl electrode as the reference electrode, a Pt wire as the auxiliary electrode, and a TC molecular imprinted polymer (MIP)-modified glassy carbon electrode (GCE, $d = 3$ mm) as the working electrode. ECL was recorded using a BPCL weak luminescence meter (Guangzhou Micro-Light Technology Co., Ltd. China). The buffer solution was configured using a PHS-3C pH meter (Shanghai Leici Instruments, China). Scanning electron microscopy (SEM; ZEISS SUPRA 55, Germany), atomic force microscopy (AFM; NT-MDT, Ntegra Prima SPM, Russia), and transmission electron microscopy (TEM; FEI Tecnai G2 F20, USA) were used to study the morphology of 2D COF. In addition, Fourier-transform infrared spectroscopy (FT-IR; Thermo Nicolet 380, USA), X-ray photoelectron spectroscopy (XPS; Thermo ESCALAB 250XI, USA), and X-ray diffraction spectra (XRD; BRUKER D8 Advance, Germany) were recorded to investigate the internal structure of 2D COF. All measurements were conducted at 25 °C. The TcPP was purchased from Frontier Scientific, Inc. (USA). *o*-PD, $ZrCl_4$, thionyl chloride, luminol and the other

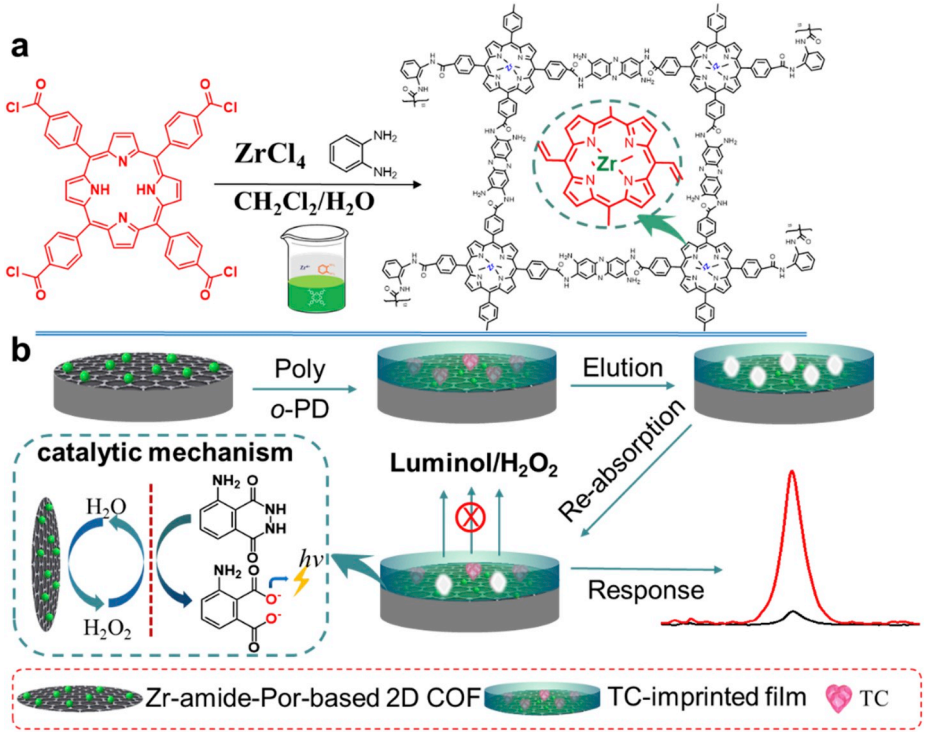

Scheme 1. Tetracycline MIECS prepared using Zr-amide-Por-based 2D COF.

convention reagents were purchased from Aladdin Reagent Co., Ltd. (China). Moreover, the TC, chloramphenicol (CAP), oxytetracycline (OTC), ampicillin (AMP), and penicillin were provided by Beijing Jinmo Quality Inspection & Technology Co., Ltd. (China). All the conventional reagents were of analytical grade and were used without further purification. All solutions were prepared using ultrapure water (18.2 MΩ cm) obtained from a Milli-Q water purification system (Millipore, USA).

2.2. Synthesis of Zr-amide-Por-based 2D COF

The TcPP (3.00 g, 3.8 mmol) was refluxed in thionyl chloride (15 mL, 0.21 mol) at 70 °C for 3 h under a N_2 atmosphere until the suspension became a dark red/brown solution. The excess thionyl chloride was removed in vacuo to obtain TcPP chloride, which was used without further purification. The chlorinated product was dissolved in dichloromethane (20 mL) for preparing the organic phase. The prepared organic phase was poured into a glass cylinder (diameter: 35 mm) at room temperature (25 °C), under N_2 atmosphere. The solution was then covered with pure water (10 mL) such that a two-phase system was formed. An aqueous solution (10 mL) of $ZrCl_4$ (2 g) and *o*-PD (1.6 g) was added gently to the water phase. After keeping the reaction system undisturbed for 12 h, a bottle green film of Zr-amide-Por-based 2D COF was generated at the interface. The obtained product was centrifuged and washed with ethanol, and was then vacuum-dried overnight at 50 °C.

2.3. Preparation of TC-MIECS

The GCE was polished by chamois leather covered with an aqueous slurry of alumina (1.0, 0.3, and 0.05 μm), and was then sequentially washed with water, ethanol, and 0.5 M H_2SO_4. Subsequently, the Zr-amide-Por-based 2D COF (20 mg) were dispersed in methanol (10 mL) by ultrasonication, and 10 μL of the resulting dispersion was dropped onto the surface of the GCE and allowed to dry at room temperature. Finally, the TC MIP film was prepared by dipping the above-mentioned electrode into the electrolyte solution of *o*-PD and TC (both 0.5 mM) in 0.02 M phosphate buffer saline (PBS; pH = 6.2), followed by which the film was subjected to 30 CV cycles over a potential range of 0 to +0.8 V at a scan rate of 50 mV/s. The non-MIP (nMIP) film was prepared using an identical procedure in the absence of TC.

The TC present in the internal cavities or membrane surface due to adsorption was removed by immersing the film for 5 min in a mixture of carbinol/acetic acid (8:1, v/v) to obtain the TC-MIECS. During rebinding, the sensor was immersed in solutions with different TC concentrations for 8 min to establish an adsorption equilibrium.

2.4. Sample pretreatment

Milk samples were purchased from a supermarket in Longhua District, Haikou City. With reference to a previous study (Zhou et al., 2012), 1 mL of milk sample was added to 1 mL of methanol and 8 mL of PBS buffer (pH 6.2), and the solution was mixed in a vortex for 30 s. The mixture was centrifuged at 5000 rpm for 5 min (0 °C). The dilution and freezing centrifugation were used to separate the fat and casein from the milk sample. The intermediate layer of serum containing no fat and casein was used as a resorption solution for subsequent experiments.

2.5. ECL measurements

The ECL signal was obtained using a luminol-H_2O_2 system. After rebinding, the ECL response was investigated in a 10 mL detector cell filled with borate saline buffer (pH 8.5, 0.02 M) containing 0.1 mM luminol and 2 mM H_2O_2. The voltage of the photomultiplier tube was set to 600 V, and the scanning potential ranged from 0 to +0.8 V.

3. Results and discussion

3.1. Characterization of Zr-amide-Por-based 2D COF

The morphologies of proposed 2D COF were fully characterized through SEM, AFM, and TEM. The internal structure of the material was

comprehensively determined through FT-IR, XPS, XRD, and HRTEM. The SEM analysis revealed the presence of multilayered sheet-like nanostructures (Fig. 1A, B, and C), which were further confirmed by TEM analysis (Fig. 1D). In particular, laminar structures were identified at the edge of the film, suggesting that the proposed 2D COF featured multilayers. Furthermore, the HRTEM clearly shows that the COF was composed of layers and orthogonal features at edges, suggesting a square crystal facet in the film (Fig. 1E and F). The internal order was observed in small domains and exhibited a lattice with a d-spacing of 0.4 nm between parallel squares. The fast Fourier transform pattern (inset of Fig. 1F) also reveals the same square periodicity. The lattice with d-spacing of 0.4 nm is attributed to the cavity of the porphyrin units, which is consistent with that reported in literature (Sahabudeen et al., 2016). The AFM measurement exhibited flat films with a thickness of 23 nm, thus demonstrating the ultra-thin character of the film (Fig. S1). Overall, the multiple analytical approaches determined the successful formation of a multilayer porous graphene sheet-like 2D COF at the liquid-liquid interface.

FT-IR, XPS, and XRD were used to further confirm the internal structure of the 2D COF. The IR data (Fig. 2A) displayed a blue shift of the carbonyl stretch from 1697 cm^{-1} in TcPP to 1660 cm^{-1} in the 2D COF. Furthermore, the appearance of the amide II band (combined absorption peak of N–H bending and C–N stretching vibrations) at 1532 cm^{-1} confirmed the formation of an amide bond because of the condensation reaction. The XPS analysis was performed to investigate the elemental composition and surface chemical states of the COF. Fig. 2B shows a representative XPS survey spectrum of Zr-amide-Por-based 2D COF, which indicates the presence of C, N, O, and Zr. Deconvolution of C 1s and N 1s (Fig. 2C and E, respectively) signals indicated the retention of the porphyrin unit in the 2D COF. The XPS spectra of C 1s displayed peaks at binding energies of 284.0, 285.0, and 288.0 eV, which corresponded to the C═C, C–H/C–C, and C–N bonds of the tetra-pyrrole macrocycle and benzene in the Zr-porphyrin coordination complexes. Additionally, the XPS N 1s spectrum showed a peak at the binding energy of 397.6 eV, indicating the coordination between Zr and N (X. Li et al., 2019). The observed 184.9 eV binding energy of Zr3d spectra also demonstrates the presence of Zr–N coordination (Fig. 2F). Furthermore, the O1s spectra (Fig. 2D) showed two peaks located at approximately 531.2 and 532.6 eV, which are attributed to N–C═O in the amide, and from the partly unreacted –COOH in the TcPP (Zhang et al., 2016). These results are consistent with the results of the FT-IR analysis, and further confirm the formation of the amide. The crystal structures of TcPP and COF were further investigated by XRD, and the results show that TcPP (Fig. S2a) has an amorphous broad peak at approximately 20°, indicating the amorphous form of porphyrin. However, The XRD pattern of Zr-amide-POR-based 2D COF (Fig. S2b) exhibits two main peaks at 3.4° and 7.5°, corresponding to the (110) and (220) facets, respectively, indicating the formation of an AA stacking structure (Wang et al., 2019). Overall, these results suggest that during the interfacial polymerization process, the Zr coordinates to the porphyrin ring, followed by which, the formation of amide bonds interconnecting the resulting complex units leads to the formation of a regular ordered 2D COF structure. Stewart et al. (2017) reported on the preparation of ordered amide COF through the devitrification of amorphous polyamide network polymers at high temperature and pressure; this resulted in the formation of 2D and 3D covalent amide frameworks. Different from high temperature and high-pressure conditions, the interfacial reaction is the key to the successful synthesis of ordered amide COF in this study.

3.2. Confirmation of electrochemical properties of Zr-amide-Por-based 2D COF/GCE

The electrochemical properties of the Zr-amide-Por-based 2D COF/GCE including conductivity, electrocatalytic activity, electrode effective area, and electrode stability were investigated. Conductivity is an important property to consider while choosing components for electrode surface-modification. For organic conductive materials, the energy difference between the highest occupied molecular orbital (HOMO) and the lowest unoccupied molecular orbital (LUMO) is a good indicator of

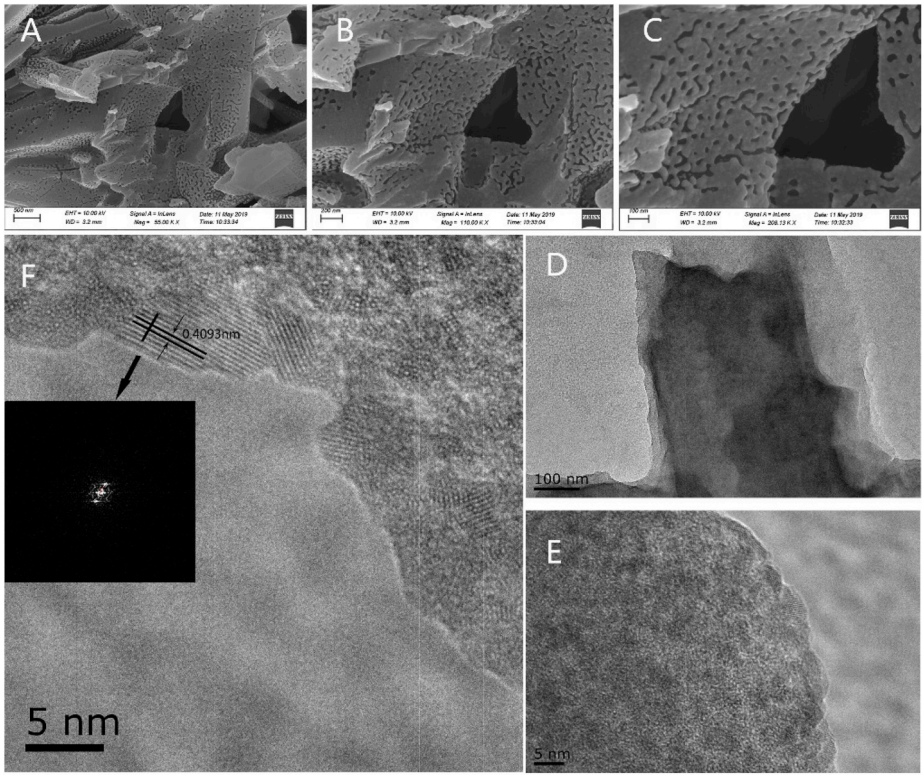

Fig. 1. SEM (A, B, and C), TEM (D) and HRTEM (E, F) of Zr-amide-Por-based 2D COF.

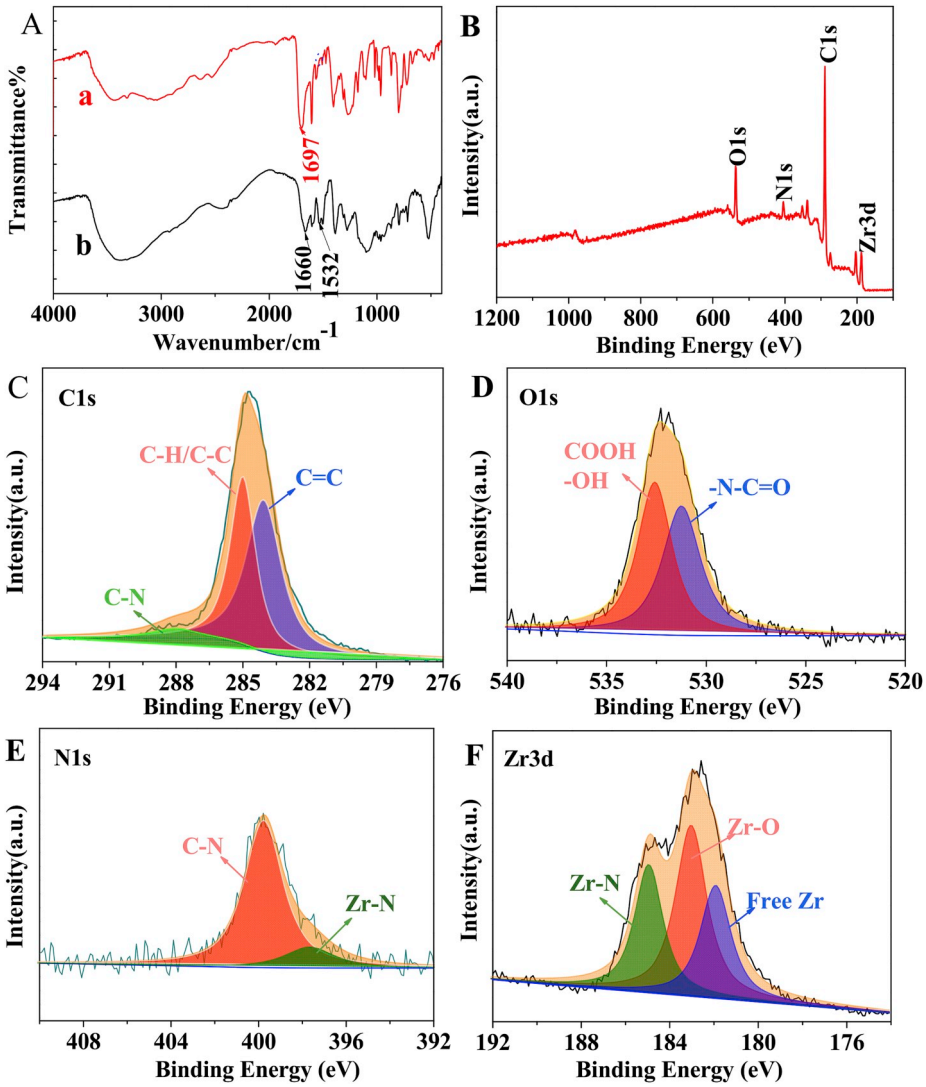

Fig. 2. FT-IR (A) and XPS survey (B). C1s (C), O1s (D), N1s (E), and Zr3d (F) spectra of Zr-amide-Por-based 2D COF.

its electrical conductivity. In this study, the HOMO-LUMO band gap of the 2D COF was measured by CV on a CHI600E workstation using a standard three-electrode system comprising an Ag/AgCl/saturated KCl electrode as the reference electrode, a Pt wire as the auxiliary electrode, and a 2D COF/GCE as the working electrode. The N, N-dimethylformamide after distillation and oxygen removal contains 0.1 M NH_4PF_6, and it was adopted as an electrolyte. The electrical scanning rate was 50 mV/s, with a scanning voltage of −2.5 to 1.5 V and 5 scanning circles. To calibrate the reference electrode, ferrocene/ferrocenium (Fc/Fc^+) redox potential was measured under the same conditions as mentioned earlier, except that the working electrode was replaced with a bare GCE. The onset reduction and oxidation potentials were −1.097 and 0.497 V (Fig. 3A), respectively, with reference to the Fc/Fc^+ redox potential. The HOMO and LUMO levels were determined to be the following: $E_{HOMO} = -[E_{ox} - E_{(Fc/Fc+)} + 4.8]$ eV and $E_{LUMO} = -[E_{red} - E_{(Fc/Fc+)} + 4.8]$ eV. Accordingly, the HOMO/LUMO energies of the 2D COF were calculated to be −5.19 and −3.59 eV, respectively, owing to which the material exhibited superior electrical conductivity than that of the reported porphyrin-based COF (Wang et al., 2019). The i-t curve can effectively reflect the catalytic decomposition efficiency of hydrogen peroxide, and was thus acquired to confirm the electrocatalytic performance of 2D COF for hydrogen peroxide (Fig. 3B). The modified electrode shows a larger step-up current indicating more H^+ production, that is, an enhancement of the catalytic decomposition effect.

The effective area of the modified electrode is an important parameter in electrochemical sensors. 5 mM Fe $(CN)_6^{3-/4}$ containing 0.1 M KCl was adopted as a probe to measure the effective area of the Zr-amide-Por-based 2D COF/GCE and bare GCE by CV at different scan rates (Goyal et al., 2010; Shahamirifard and Ghaedi, 2019). As shown in Fig. S3, the peak current is proportional to the $\nu^{1/2}$ in the range of 0.01–0.2 V/s, indicating a diffusion control process. Acoording to the slope of Ip - $\nu^{1/2}$ plot (Ip (A) = 2.81×10^{-4} $\nu^{1/2}$ - 2.05×10^{-5}, $R^2 = 0.9953$) and Randles–Sevcik equation ($Ip = 2.69 \times 10^5$ $n^{3/2}$ A_{eff} $D^{1/2}$ $\nu^{1/2}$ C), the effective area of Zr-amide-Por-based 2D COF/GCE was estimated to be 7.58 mm^2. It was found that the effective area of the modified electrode is ~1.64 times larger than that of the bare GCE (4.61 mm^2), which may be attributed porous structure of Zr-amide-Por-based 2D COF. In Randles–Sevcik equation, Ip is the peak current (A), For 5 mM Fe $(CN)_6^{3-/4-}$ containing 0.1 M KCl, n = 1, $D = 7.6 \times 10^{-6}$ cm^2 s^{-1}, A_{eff} is the effective area (cm^2), C is the concentration of Fe $(CN)_6^{3-/4-}$ in mol cm^{-3} and ν is the scan rate (V/s).

Leaching studies were conducted for confirming the stability of the modified electrode. The prepared modified electrode was immersed in a luminescent cell containing borate saline buffer (pH 8.5, 0.02 M), 0.1 mM luminol, and 2 mM H_2O_2 for 90 min, and the ECL intensity was recorded per 10 min. The results showed that the ECL intensity change was below 5% within 90 min (Fig. S4), indicating that the modified

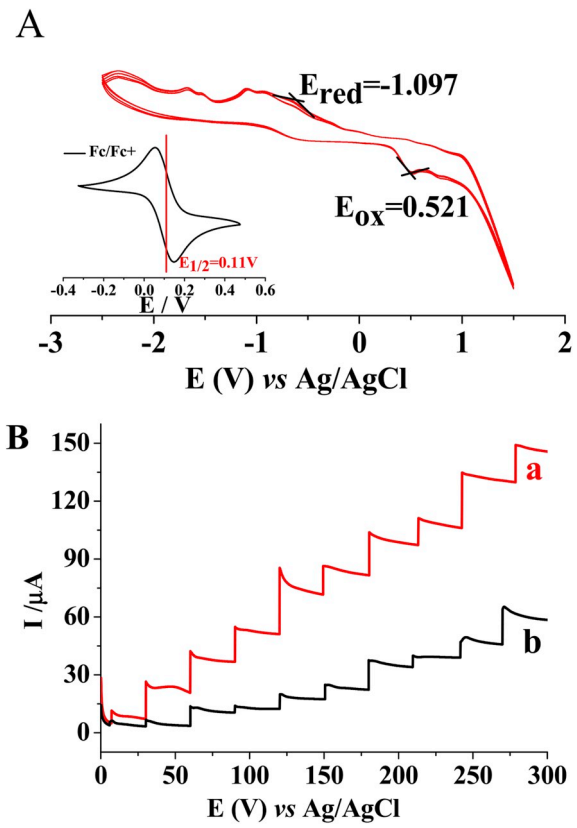

Fig. 3. A: CV measurement of Zr-amide-Por-based 2D COF (inst: CV of Fc/Fc^{+} couple used for calibrating the pseudo-reference electrode.); B: Typical current–time responses of the 2D COF/GCE (a) and bare GCE (b) to the successive additions of H_2O_2 in steps of 0.2 mM at an applied potential of −0.8 V.

electrode has good stability. This should be attributed to the ultra-thin features of the COF, resulting in electrode adhesion similar to that in graphene. These remarkable results indicate that the prepared 2D COF is predictable and offers unparalleled advantages as a component for electrode modification.

3.3. Preparation of the TC-MIP and nMIP film

The previous sections presented the preparation and evaluation of the novel COF, and in this section, we focus on TC detection. A TC-MIP film was prepared on the surface of the 2D COF-modified electrode. CV was carried out in an electrolytic cell containing 0.5 mM *o*-PD, 0.5 mM TC, and 0.02 M PBS. As the polymerization progresses, the oxidation peak current of *o*-PD gradually decreases, indicating the formation of a dense nonconductive polymer film on the electrode surface (Fig. S5A). The surface features of the MIP film were further observed through SEM. The images showed the formation of a dense and uniform membrane on the surface of the COF layer (Fig. S5C), indicating the successful preparation of the TC-MIP film. A nMIP film, which did not contain TC, was prepared under the same conditions. The CV analysis of these two membranes indicated no significant difference; this confirms that TC does not participate in the polymerization reaction and is immobilized in the imprinted membrane due to noncovalent interactions such as hydrogen bonding and van der Waals forces (Fig. S5B). The topographical features of nMIP film did not show significant differences with those of the MIP films, and this may be attributed to the inability of SEM to provide capture information at a molecular level (Fig. S5D).

3.4. Electrochemical characterization of the fabricated sensor

Potassium ferricyanide is an effective electrochemical probe for revealing electrode interface changes. Therefore, we monitored the sensor construction through CV and EIS measurements. The CV measurements were performed over a potential range of –0.2 to +0.6 V at a scan rate of 100 mV/s, whereas the EIS measurements were performed at a potential of 0.19 V over a frequency range of 100 mHz to 100 kHz with an alternating voltage of 5 mV. The experiments were conducted using the 2D COF modified electrode, bare GCE, and TC-MIP films before and after template removal, and after rebinding with 5 pM solution of TC. The nMIP film before and after elution was also included in the study.

A current increase was observed between curves a and b, as shown in Fig. 4A, indicating that the 2D COF modified electrode maintains good electron transport capability. However, the dramatic current decrease from curves b to c indicates the formation of a nonconductive and compact MIP film on the surface of the modified electrode. After elution, the release of TC from the imprinted cavities increased the electron transfer channel, as reflected by the increase in the current from curve c to d. The continuous rebinding of TC in the recognition cavities resulted in partial electron channel blockage and induced a current decrease (curve e). Moreover, despite the formation of a nonconductive poly-*o*-PD membrane, which was indicated by the current observed for the nMIP film (curve f), an almost constant current was found after elution, which was ascribed to the absence of target molecules in nMIP and their inability to provide electron transfer channels.

The variations in electrode interface impedance during sensor construction were also monitored closely. The obtained results were analyzed using a Randles equivalent circuit (insert of Fig. 4B), where R_s is the electrolyte resistance, C_{dl} is the interface capacitance, R_{ct} is the charge (electron) transfer resistance and Z_w is the Warburg impedance. The typical impedance data are presented in the form of the Nyquist plot and relies on a semicircular region at higher frequencies corresponding to the interfacial charge transfer process and a linear part at lower frequency range representing the diffusion process. The semicircle diameter in the Nyquist plot corresponds to the charge transfer resistance (R_{ct}), which reflects the electrontransfer kinetics of the redox probe at the electrode surface. Fig. 4B shows that a slight decrease in R_{ct} was observed after modification of 2D COF (curve b). An obvious resistance increase, observed after polymerization, reflected the high resistance of electron transfer to the redox probe (curve c) and confirmed the formation of a dense nonconductive MIP film. Nevertheless, a decrease in resistance was observed when template molecules were removed from the MIP (curve d), and the remarkable increase of semicircle diameter, observed from curve d to e indicated the re-blockage of imprinted cavities or channels after template rebinding.

The ECL response of the sensor to the luminol/H_2O_2 under different states can also reflect the sensor interface changes (Fig. 4C). After modifying the COF, a current amplification close to 8 times that of the bare GCE (curve a to b) was observed; this might be due to the outstanding electrical conductivity and efficient electron transfer capability of the porous structure. In addition, the coordination of Zr has a synergistic effect on the catalysis of hydrogen-peroxide decomposition. Fig. S6 shows a plausible mechanism for the ECL catalysis, wherein the 2D COF catalyzes the cleavage of the O–O bond in H_2O_2 into two $HO^{\bullet}$ radicals, which react with luminol and HO_2^- anions to afford luminol radicals ($L^{\cdot-}$) and superoxide radical anions ($O_2^{\cdot-}$), resulting in ECL amplification. During subsequent sensor construction, the ECL maintains a similar trend to CV or EIS. Thus, the results of electrochemical characterization of CV, EIS, and ECL confirmed that the prepared sensor was constructed successfully on the GCE surface.

3.5. Optimization of analytical conditions

Multiple-sensor construction conditions, including the pH of the

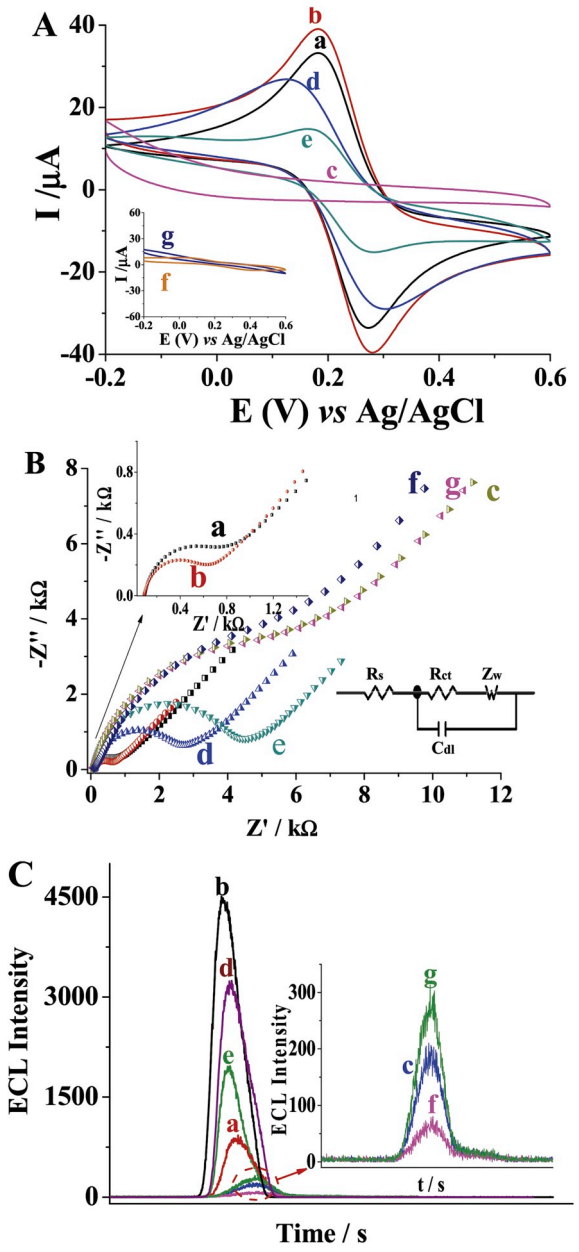

Fig. 4. TC MIECS construction monitoring by CV (A), EIS (B) and ECL (C). (The CV and EIS were performed in 5 mM Fe $(CN)_6^{3-/4}$ solution containing 0.1 M KCl; ECL is performed in borate saline buffer (pH 8.5, 0.02 M) containing 0.05 mM luminol and 2 mM H_2O_2; a: bare GCE, b: Zr-amide-Por-based 2D COF/GCE, c: TC-MIP film, d: TC-MIP film after template removal, e: TC-MIP film after rebinding with 5 pM TC, f: nMIP film, and g: nMIP after elution).

polymerization and luminescence cells, elution time, resorption time, and amount of hydrogen peroxide, were optimized. The pH of the polymeric base has an important effect on the formation of polymeric membranes. In this study, PBS with a pH range of 5.6–8.0 was investigated, and the elution current was used as an evaluation index (5 mM potassium ferricyanide solution as a probe). The PBS buffer with a pH of 6.2 resulted in a maximum elution current when the other conditions were consistent (Fig. S7), which may be related to the stability of TC molecules in a weakly acidic environment. Upon optimizing the elution time, the ECL intensity gradually increased with increasing elution time and reached its maximum at 5 min (Fig. S8a). The resorption time was also investigated. Over time, the template molecules were observed to bind again, gradually blocking the mass-transfer channel of the imprinted membrane, because of which the reabsorption intensity reached a stable value at 8 min (Fig. S8b). The pH in the luminescence cell and the amount of hydrogen peroxide are important conditions influencing the final signal acquisition of the sensor. After performing optimization experiments, boric acid–borax buffer (pH 8.5) (Fig. S9a) and 2 mM hydrogen peroxide (Fig. S10) were used as the optimum conditions for subsequent experiments. Moreover, the effects of different buffer solutions on luminescent probes were investigated. Different buffers, such as borate, Tris-HCl, Britton-Robison, and phosphate buffers, were tested and the results showed a similar changing trend with slightly different effect on the luminol/H_2O_2 ECL intensity (Fig. S9). Finally, the borate buffer was chosen because the most stable ECL signal could be obtained in this buffer.

3.6. Adsorption kinetic study

The adsorption kinetic parameters of the TC-MIECS was further confirmed by the Langmuir adsorption model (Tan et al., 2015), which is typical for the adsorption of imprinting polymers. The following equation was used to explore the Langmuir adsorption kinetic process:

$$\Delta ECL_{Re} = \Delta ECL_{Sa} * \frac{t}{k+t}$$

where $\Delta ECL_{Re}(a.u)$ is the ECL intensity change response to the re-adsorption time (t; s), $\Delta ECL_{Sa}(a.u)$ is the ECL intensity change response of saturation capacity, and k (s) is the constant kinetic rate. Fig. S11 presents the ΔECL_{Re} - t plot of MIECS and non-MIECS. The k values of MIECS sensor is larger than that of non-MIECS as shown in Table S1. That might be attributed to Zr-amide-Por-based 2D COF, which plays an important role in promoting electron transfer and increasing the special recognition cavities of TC. Therefore, the imprinted effect produces many rebinding sites to TC but only weak adsorption to the non-template molecules on the film surface.

3.7. Analytical performance

The fabricated sensor was used for TC quantitation under optimal conditions, and the ECL intensity was found to linearly decrease with an increase in TC concentration over the 5–60 pM range (Fig. 5), and data were used to construct a regression equation, represented by $\Delta ECL = 110.24\,C\ (\mathrm{pM}) - 11.77$ ($R^2 = 0.991$). The sensor detection limit was calculated as 2.3 pM (3δ/K, n = 11).

The detection repeatability was investigated by measuring TC at three different concentrations (5, 20, and 40 pM). All experiments were performed in triplicate, and notably, all obtained relative standard deviations (RSDs) did not exceed 6.7%, indicating acceptable reproducibility. Furthermore, the response stability of the optimized sensor was

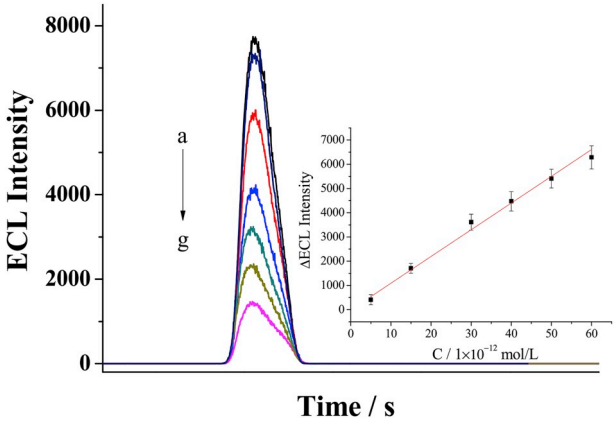

Fig. 5. ECL responses of the proposed sensor to different concentrations of TC (a–g: 0, 5, 15, 30, 40, 50, and 60 pM, respectively). Inset: Calibration plot of ΔECL intensity vs. TC concentration, with error bars corresponding to $n = 3$.

evaluated using 12 consecutive cyclic potential scans (Fig. S12), and the obtained very low RSD of the concomitant ECL intensity change (0.94%) indicated excellent stability. The obtained results were compared with those of the recently reported TC electrochemical sensors (summarized in Table S2). The data indicated that the prepared sensor has some limitations in the linear range but shows a higher sensitivity and acceptable stability. It is also worth mentioning that the proposed sensor shows significant advantages in fabrication time and analysis time compared to recently reported aptamer electrochemical sensors.

3.8. Cross-reactivity studies

Analogues of the analyte (CAP, OTC, AMP, and penicillin; $C_{analogue} = 10$ nM) and common ions (Na^+, K^+, Ca^{2+}, Mg^{2+}, and Fe^{3+}; $C_{ion} = 1$ μM), and corresponding TC–interferent(s) mixtures ($C_{TC} = 50$ pM), were examined with respect to cross-selectivity with the fabricated sensor. The ΔECL intensity was obtained for the analogues and interfering species with and without TC, under optimized conditions. As shown in Fig. S12, the results clearly demonstrate that because of the good selectivity of the molecularly imprinted cavities, the developed TC sensor has good anti-interference ability. More importantly, common coexisting ions do not affect the sensor's response to the target molecule, showcasing the adaptability of the sensor for real-world applications. In addition, a parallel study on cross-reactivity of interferent(s) in the presence of TC is feasible with the proposed sensor. The binary mixtures tested in this work were in high concentration ratios, and the corresponding ECL response for TC was highly quantitative without any contributions from interferents. These results demonstrate the strong applicability of the developed sensor for reliable monitoring of TC levels in animal-derived foods.

3.9. Real sample analysis

To assess the applicability and gain insight into the recovery of TC in real-world applications, known quantities (10, 30, and 60 pM) of TC were spiked in milk samples, which were measured by TC-MIECS (Table S3). It is noteworthy that the percentage recovery values of TC in these samples ranged from 94.0% to 103.5%, which further attests to the applicability of the developed electrode for detecting TC in real biological samples. The RSD for the measurements was less than 7.0%.

4. Conclusions

A facile liquid-liquid interface synthesis method was used for the preparation of an ordered amide COF. The unique electrocatalytic performance of COF was used for the development of a TC molecular imprinted ECL sensor. While the developed COF and sensor displayed remarkable performance characteristics, some challenges, such as the inevitable separation of byproducts brought about from the interfacial polymerization process, remain to be addressed. While great progress has been achieved in the preparation of COF at the interfaces, the focus on obtaining a single layer of COF will be an interesting research direction for the further evolution of this area of work. Overall, the prepared single-layer COF is predictable and facilitates performance improvement in the field of electrocatalysis.

Declaration of competing interest

The authors declare that they have no known competing financial interests or personal relationships that could have appeared to influence the work reported in this paper.

CRediT authorship contribution statement

Xionghui Ma: Conceptualization, Validation, Data curation, Formal analysis, Writing - original draft. **Chaohai Pang:** Formal analysis, Data curation. **Shuhuai Li:** Funding acquisition, Conceptualization, Writing - review & editing. **Yuhao Xiong:** Funding acquisition, Formal analysis, Data curation. **Jianping Li:** Supervision, Writing - review & editing. **Jinhui Luo:** Supervision, Writing - review & editing. **Yan Yang:** Writing - review & editing.

Acknowledgments

This work was supported by the Central Public-interest Scientific Institution Basal Research Fund for the Chinese Academy of Tropical Agricultural Sciences (No.1630082017002 and 1630082017001), Integration and Demonstration of Key Technologies for Rice-Cash Crop Rotation System, High Level Innovation Teams of Guangxi Colleges & Universities/Outstanding Scholars Program (Guijiaoren[2018]35) and Financial Fund of the Ministry of Agriculture and Rural Affairs, P. R. of China (NFZX2018).

Appendix A. Supplementary data

Supplementary data to this article can be found online at https://doi.org/10.1016/j.bios.2019.111734.

References

El Alami El Hassani, N., Baraket, A., Boudjaoui, S., Taveira Tenório Neto, E., Bausells, J., El Bari, N., Bouchikhi, B., Elaissari, A., Errachid, A., Zine, N., 2019. Biosens. Bioelectron. 130, 330–337.
Cherkashina, K., Vakh, C., Lebedinets, S., Pochivalov, A., Moskvin, L., Lezov, A., Bulatov, A., 2018. Talanta 184, 122–127.
Deblase, C.R., Hernández-Burgos, K., Silberstein, K.E., Rodríguez-Calero, G.G., Bisbey, R. P., Abruña, H.D., Dichtel, W.R., 2015. ACS Nano 9, 3178–3183.
Devkota, L., Nguyen, L.T., Vu, T.T., Piro, B., 2018. Electrochim. Acta 270, 535–542.
Díaz-Quiroz, C.A., Francisco Hernández-Chávez, J., Ulloa-Mercado, G., Gortáres-Moroyoqui, P., Martínez-Macías, R., Meza-Escalante, E., Serrano-Palacios, D., 2018. J. Chromatogr. B 1092, 386–393.
Gao, W., Liu, Z., Qi, L., Lai, J., Kitte, S.A., Xu, G., 2016. Anal. Chem. 88, 7654–7659.
Goyal, R.N., Gupta, V.K., Chatterjee, S., 2010. Sens. Actuators B Chem. 149, 252–258.
Grande-Martínez, Á., Moreno-González, D., Arrebola-Liébanas, F.J., Garrido-Frenich, A., García-Campaña, A.M., 2018. J. Pharm. Biomed. Anal. 155, 27–32.
Guidi, L.R., Santos, F.A., Ribeiro, A.C.S.R., Fernandes, C., Silva, L.H.M., Gloria, M.B.A., 2018. Food Chem. 245, 1232–1238.
Huang, J., Xie, Z., Xie, Z., Luo, S., Xie, L., Huang, L., Fan, Q., Zhang, Y., Wang, S., Zeng, T., 2016. Anal. Chim. Acta 913, 121–127.
Khatioda, R., Talukdar, D., Saikia, B., Bania, K.K., Sarma, B., 2017. Catal. Sci. Technol. 7, 3143–3150.
Li, F., Yu, Z., Han, X., Lai, R.Y., 2019. Anal. Chim. Acta 1051, 1–23.
Li, S., Yin, G., Zhang, Q., Li, C., Luo, J., Xu, Z., Qin, A., 2015. Biosens. Bioelectron. 71, 342–347.
Li, X., Zhang, Y., Wang, W., Meng, J., Li, K., Lin, W., Peng, Z., Wan, J., Hu, Z., 2019. Int. J. Hydrogen Energy 44, 18072–18082.
Liu, J., Zhang, Y., Jiang, M., Tian, L., Sun, S., Zhao, N., Zhao, F., Li, Y., 2017. Biosens. Bioelectron. 91, 714–720.
Liu, X., Huang, D., Lai, C., Zeng, G., Qin, L., Zhang, C., Yi, H., Li, B., Deng, R., Liu, S., Zhang, Y., 2018. TrAC Trends Anal. Chem. 109, 260–274.
Liu, Z., Ou, J., Wang, H., You, X., Ye, M., 2016. ACS Appl. Mater. Interfaces 8, 32060–32067.
Ma, X., Li, S., Pang, C., Xiong, Y., Li, J., 2018. Microchim. Acta 185, 546.
Moreno-González, D., Krulišová, M., Gámiz-Gracia, L., García-Campaña, A.M., 2018. Electrophoresis 39, 608–615.
Moudgil, P., Bedi, J.S., Aulakh, R.S., Gill, J.P.S., Kumar, A., 2019. Food Anal. Methods 12, 338–346.
Mulzer, C.R., Shen, L., Bisbey, R.P., McKone, J.R., Zhang, N., Abruña, H.D., Dichtel, W. R., 2016. ACS Cent. Sci. 2, 667–673.
Sahabudeen, H., Qi, H., Glatz, B.A., Tranca, D., Dong, R., Hou, Y., Zhang, T., Kuttner, C., Lehnert, T., Seifert, G., Kaiser, U., Fery, A., Zheng, Z., Feng, X., 2016. Nat. Commun. 7, 1–8.
Shahamirifard, S.A., Ghaedi, M., 2019. Biosens. Bioelectron. 141, 111474.
Shahamirifard, S.A., Ghaedi, M., Razmi, Z., Hajati, S., 2018. Biosens. Bioelectron. 114, 30–36.
Sheng, W., Chang, Q., Shi, Y., Duan, W., Zhang, Y., Wang, S., 2018. Microchim. Acta 185, 404.
Shumyantseva, V.V., Bulko, T.V., Sigolaeva, L.V., Kuzikov, A.V., Archakov, A.I., 2016. Biosens. Bioelectron. 86, 330–336.
Stewart, D., Antypov, D., Dyer, M.S., Pitcher, M.J., Katsoulidis, A.P., Chater, P.A., Blanc, F., Rosseinsky, M.J., 2017. Nat. Commun. 8, 1102.
Sun, Q., Aguila, B., Perman, J., Earl, L.D., Abney, C.W., Cheng, Y., Wei, H., Nguyen, N., Wojtas, L., Ma, S., 2017. J. Am. Chem. Soc. 139, 2786–2793.
Tan, X., Hu, Q., Wu, J., Li, X., Li, P., Yu, H., Li, X., Lei, F., 2015. Sens. Actuators B Chem. 220, 216–221.

Wang, C., Chen, R., Shi, J.-L., Ma, Y., Lin, G., Lang, X., 2019. Angew. Chem. Int. Ed. 58, 6430–6434.
Xiong, Y., Chen, S., Ye, F., Su, L., Zhang, C., Shen, S., Zhao, S., 2015. Chem. Commun. 51, 4635–4638.
Xiong, Y., Qin, Y., Su, L., Ye, F., 2017. Chem. Eur J. 23, 11037–11045.
Yang, H., Zhang, S., Han, L., Zhang, Z., Xue, Z., Gao, J., Li, Yongjun, Huang, C., Yi, Y., Liu, H., Li, Yuliang, 2016. ACS Appl. Mater. Interfaces 8, 5366–5375.
Zhang, J., An, X., Lin, N., Wu, W., Wang, L., Li, Z., Wang, R., Wang, Y., Liu, J., Wu, M., 2016. Carbon 100, 450–455.
Zhang, S., Yang, Q., Wang, C., Luo, X., Kim, J., Wang, Z., Yamauchi, Y., 2018. Adv. Sci. 5, 1801116.
Zhang, X., Song, C., Yang, K., Hong, W., Lu, Y., Yu, P., Mao, L., 2018. Anal. Chem. 90, 4968–4971.
Zhou, D., Tan, X., Wu, H., Tian, L., Li, M., 2018. Angew. Chem. Int. Ed. 58, 1376–1381.
Zhou, L., Li, D.J., Gai, L., Wang, J.P., Li, Y.B., 2012. Sens. Actuators B Chem. 162, 201–208.
Zhou, Y., Yang, Q., Zhang, D., Gan, N., Li, Q., Cuan, J., 2018. Sens. Actuators B Chem. 262, 137–143.